JMEPEG (2020) 29:2531–2541
https://doi.org/10.1007/s11665-020-04738-5

1059-9495/$19.00

Effects of the Addition of Cu and Ni on the Corrosion Behavior of Weathering Steels in Corrosive Industrial Environments

Tianyi Zhang, Wei Liu, Zun Yin, Baojun Dong, Yonggang Zhao, Yueming Fan, Junsheng Wu, Zhan Zhang, and Xiaogang Li

(Submitted April 26, 2019; in revised form February 28, 2020; published online March 18, 2020)

The effect of Cu and Ni content on the corrosion behaviors of weathering steels in a corrosive atmosphere was investigated using electrochemical measurement techniques, such as electrochemical impedance spectroscopy and linear polarization resistance methods. Scanning electron microscopy with energy-dispersive spectrometry (EDS) and x-ray diffraction (XRD) were used to analyze the samples. The corrosion rates, which are above 2.0 mm a^{-1} at 48 h and approximately 1.12 mm a^{-1} at the range of 144-240 h, show that Cu and Ni slowed down the electrochemical reaction at the initial corrosion stage. With an increasing immersion time, the protective properties of the rust layer exhibited an increase in its impedance, and it was enhanced compared to that in the initial stage. The enrichment phenomenon of Cu and Ni elements in the inner rust layer was more evident in the 0.4Cu-0.4Ni and 0.7Cu-0.7Ni steels than that of 0.3Cu-0.3Ni steel after 240 h. The XRD and EDS results show that the inner rust layer contained compositions of CuO and Ni compounds, which filled up the pores located on the corrosion products contributing to the densification of the rust layer.

Keywords corrosive atmosphere, electrochemical impedance spectroscopy, weathering steel, x-ray diffraction

1. Introduction

Low-alloy mild steels, particularly weathering steels (WSs), have been extensively used as structural materials for applications in the fields of construction, transport, industrial equipment, etc., due to their excellent mechanical and weldability properties. Corrosion resistance is required to maintain these advantages as WSs are mostly used in exposed corrosive conditions such as coastal or highly polluted industrial areas, where the atmosphere corrosion is severe (Ref 1-3). To improve the protection properties of the corrosion products formed on WS surfaces, alloying elements, such as Cu, Ni, and Cr, were added to improve the corrosion resistance of bare steel surfaces (Ref 4, 5). Previous studies have reported that the results from dry–wet alternating cycles or industrial water immersion experiments with copper steels show that low-alloy steels with the presence of Cu (0.28-0.3 wt.%) and Ni (0.5-0.65 wt.%) have twice the corrosion resistance than carbon steels. This verifies that Cu-Ni mild steels possess good resistance against atmospheric corrosion (Ref 6, 7). Chen et al. (Ref 8) investigated the corrosion mechanism of Q235 mild steel exposed in Shenyang City in northeast China, although the relationship between the corrosion resistance of rust layer and the alloying elements content had not been explored in depth. It has also been shown that the corrosion behaviors in the different corrosion stages were greatly affected by environmental factors, without elaborating on the specific functions of the corrosion products in each stage (Ref 9-11). Thus, it is necessary to investigate the evolution mechanisms of the alloying elements in the corrosion rust layers produced in an industrial atmosphere environment.

COR-TEN steels, a kind of high-strength low-alloy steel containing Cu (0.25-0.55 wt.%) and Ni (≤ 0.65 wt.%), were launched by US Steel in 1933; they were characterized with good performance in corrosion resistance and tensile strength (Ref 2, 12). COR-TEN steels present high corrosion rates when used in industrialized areas due to the high SO_2 concentrations in these areas (Ref 13-15). Although several studies have shown WSs present good resistance to atmosphere corrosion (Ref 11-13, 16-18), few investigations discussed the possible limitations of the application of COR-TEN steels in industrial environments where SO_2 is present. Few studies (Ref 6-8) have shown that severe corrosion behavior is present in WSs placed in environments with higher SO_2 concentrations. It was revealed that SO_2 could accelerate the rust formation by promoting phase transformation, producing a more homeostatic structure of goethite (α-FeOOH) to improve the protective properties of the rust layer (Ref 14, 15). Thus, the effect of SO_2 on the corrosion behavior has not been fully clarified and should be further discussed. In addition, the effects of adding alloying elements, such as Cu and Ni, to the corrosion resistance of the steel should also be investigated.

The main objective of this research was to obtain COR-TEN steels with high-cost performance and corrosion resistance in corrosive environments by changing the chemical composition. The effects of Cu and Ni on the properties of the rust layers of WSs after being tested in a simulated industrial environment were investigated to reveal the evolution of the corrosion rates

Tianyi Zhang, Wei Liu, Zun Yin, Baojun Dong, Yonggang Zhao, Yueming Fan, Junsheng Wu, Zhan Zhang, and **Xiaogang Li**, Corrosion and Protection Center, Key Laboratory for Corrosion and Protection (MOE), Institute for Advanced Materials and Technology, University of Science and Technology Beijing, Beijing 100083, China. Contact e-mail: weiliu@ustb.edu.cn.

Table 1 Chemical compositions of the three low-alloy steels (wt.%)

Elements	C	Si	P	Mn	S	Cu	Ni	Cr	Ti	Fe
Steel 0.7Cu-0.7Ni	0.045	0.30	0.081	0.41	0.005	0.74	0.74	0.30	0.02	Bal.
Steel 0.4Cu-0.4Ni	0.045	0.30	0.081	0.41	0.005	0.40	0.35	0.32	0.02	Bal.
Steel 0.3Cu-0.3Ni	0.09	0.30	0.081	0.41	0.005	0.28	0.27	0.48	0.02	Bal.

Table 2 Parameters of the alternate immersion tests

Experimental variables	
Soaking time, min	10
Drying time, min	50
The tank temperature, °C	27 ± 1
The temperature inside the box, °C	27 ± 1
Average relative humidity, %	30
One cycle time, h	48
Total cycle time, h	240

Annotation: One cycle includes the soaking and drying processes

and compositions of the corrosion products using scanning electron microscopy (SEM) equipped with energy-dispersive spectrometry (EDS) and x-ray diffraction (XRD). Electrochemical impedance spectroscopy (EIS) and linear polarization resistance (LPR) were conducted to study the electrochemical evolution on the rust layers.

2. Materials and Methods

2.1 Materials and Preparation

Two high-strength (~ 400 MP) low-alloy steels, named as 0.7Cu-0.7Ni steel and 0.4Cu-0.4Ni steel, were investigated in this work. A traditional weathering steel 0.3Cu-0.3Ni, namely COR-TEN A steel (09CuPCrNi), was used as the comparative steel. The chemical compositions of the three steel samples are listed in Table 1.

Three specimens were performed by alternate immersion corrosion tests for corrosion rate measurements, rust analyses, and electrochemical measurements. Specimens were cut to obtain two sizes of 50 mm × 40 mm × 5 mm and 10 mm × 10 mm × 2 mm. Each specimen was ground with water sandpapers up to a grit size of 1200, degreased by acetone, and dried at 25 °C before corrosion tests.

2.2 Alternate Immersion Corrosion Tests

The corrosive industrial environment was simulated using an alternate immersion accelerated tests using a multifunctional cyclic corrosion test chamber (ATLAS CCX2000). The corrosion electrolyte used was 0.085 mol/L $NaHSO_3$ solution where the ion concentration was equal to 0.5% NaCl solution used for simulating ocean environments. The experimental parameters are shown in Table 2. After the corrosion tests, a stereomicroscope (LEO-1450) was employed to observe the macromorphologies of the corroded samples.

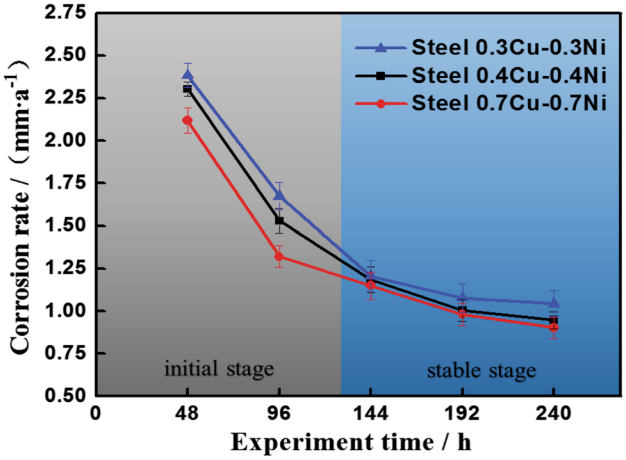

Fig. 1 Corrosion rates of the steel as a function of the experiment time of the alternate immersion corrosion tests

The corrosion rates of the three low-alloy steels after the corrosion tests were calculated using the corrosion rate v_i (mm a^{-1}) Eq 1 (Ref 5, 12):

$$v_i = 8.76 \times \frac{\Delta w}{s \cdot \rho \cdot t} \quad \text{(Eq 1)}$$

where Δw is the weight loss (g), t is the corrosion test time (h) and s and ρ (equal to 7.85) are the exposed area (m^2) and the density (g m^{-3}) of the specimen, respectively. The corrosion products formed on the specimens were chemically removed by immersing the specimens in a solution containing 500 mL hydrochloric, 500 mL distilled water, and 3.5 g hexamethylenetetramine. The specimens were magnetically stirred in the solution for ~ 10 min at 25 °C. After the rust layers were completely removed, the specimens were rinsed with distilled water, dried with warm air, and then weighed to determine their mass loss, which was used to calculate the corrosion rate. The macro-morphologies of the specimens after the removal of the rust layers were also investigated through stereomicroscopy.

2.3 Characterization of the Rust Layer

The surface and cross-sectional morphologies of the rust layers formed after the alternate immersion tests were investigated using SEM (FEI Quant250 environmental, USA) equipped with EDS for the element distribution analysis. The phase composition of the rust layers on the specimens was analyzed by XRD (Smart Lab 9kw diffractometer, Japan) with a Cu Kα target under 40 kV, and an incident angle range of 10°-100° with a scanning rate of 2°/min.

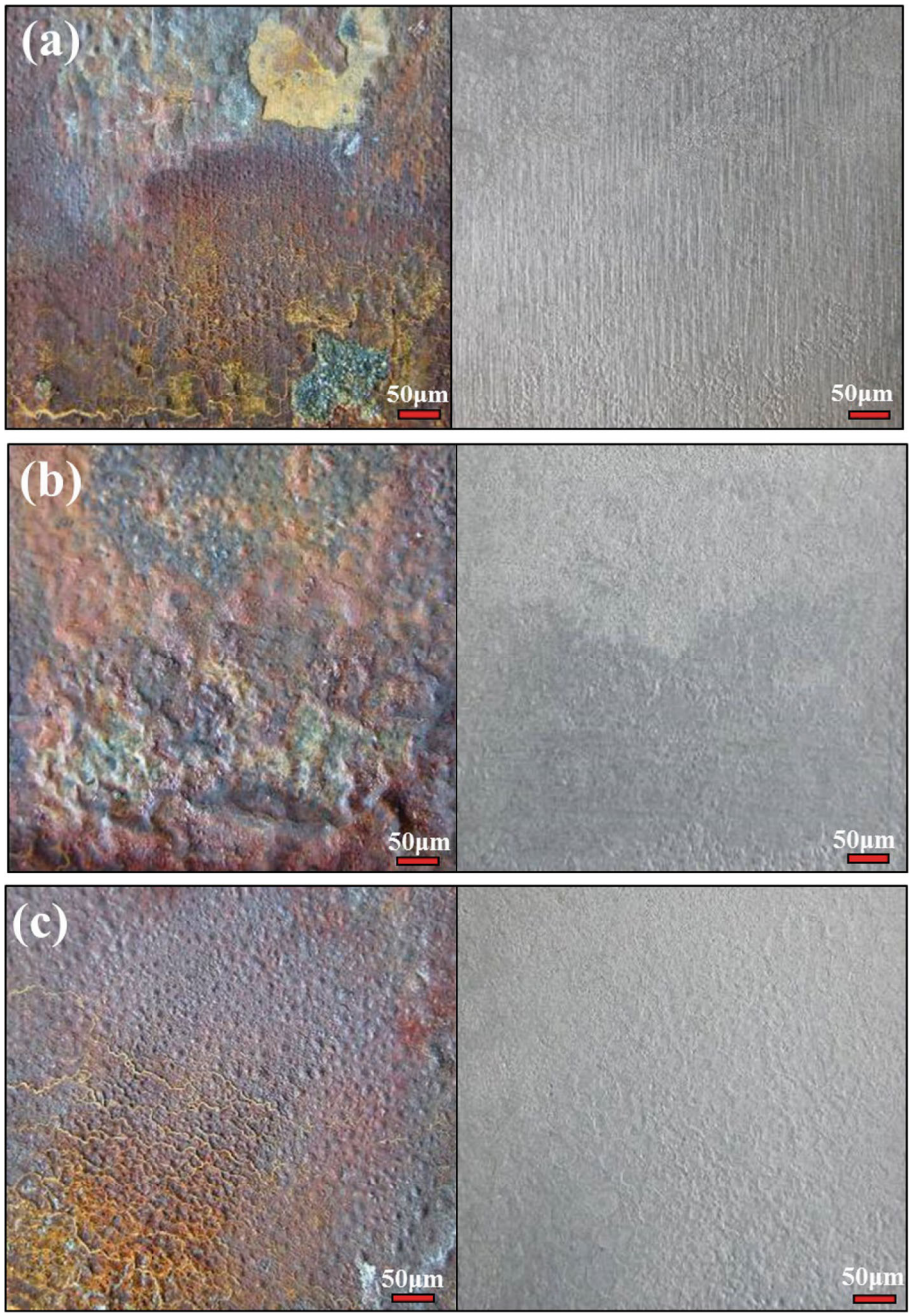

Fig. 2 Surface appearances of the rust after 240-h corrosion tests and steel surfaces after rust removal: (a) 0.3Cu-0.3Ni steel, (b) 0.4Cu-0.4Ni steel, and (c) 0.7Cu-0.7Ni steel

2.4 Electrochemical Measurements

The electrochemical measurements were conducted in a conventional three-electrode cell with a Pt plate as a counter electrode and a saturated calomel electrode (SCE) as a reference electrode in a 0.085 mol/L $NaHSO_3$ solution. The surfaces of the specimen were gradually ground with water sandpapers up to a grit size of 2000, degreased with acetone, and dried. The as-prepared and rusted steel samples through each cycle (48, 96, 144, 192, and 240 h) in the corrosion tests were employed as working electrodes with an exposed area of 1 cm^2. Electrochemical impedance spectroscopy (EIS) was conducted over a frequency range from 100 kHz to 10 mHz using 10 mV_{SCE} sinusoidal potential modulations around corrosion potential with eight points per decade. It is worth mentioning that before EIS, all samples were immersed in the solution for 30 min for stabilization. Linear polarization curves were obtained after the EIS tests at a scanning rate of 0.1667 mV/s with a scanning range from − 10 to 10 mV_{OCP}. All electrochemical tests were conducted using an electrochemistry workstation (PGSTAT302N, Metrohm, Switzerland), and the obtained experimental data were analyzed using the ZSimpWin software.

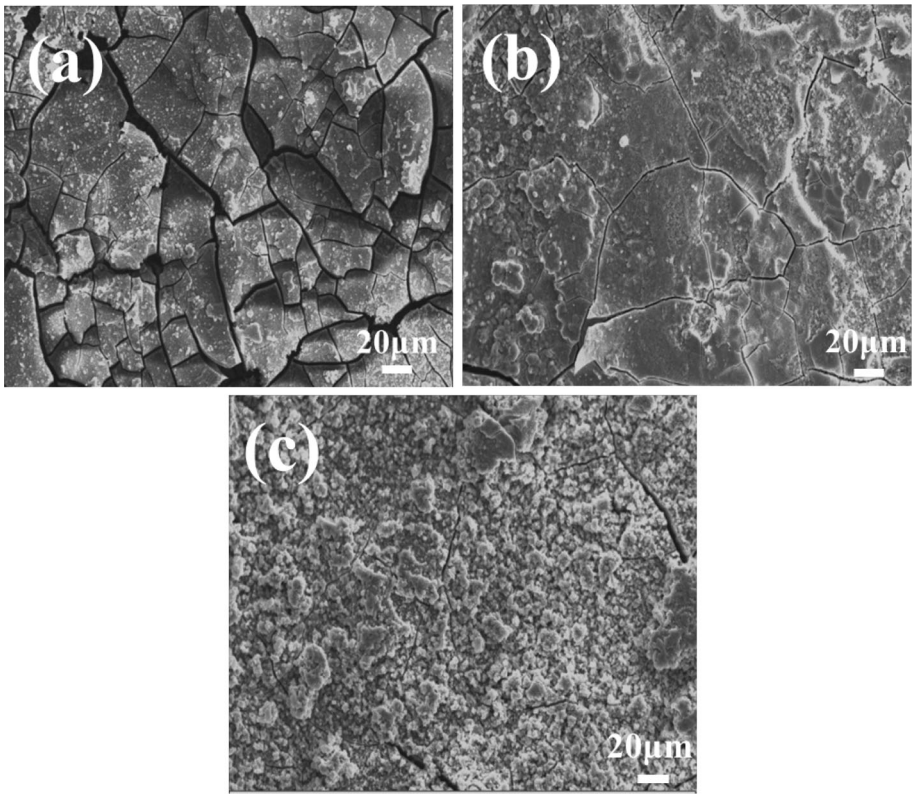

Fig. 3 Surface morphologies of the corrosion products on the investigated steels after 240-h corrosion tests: (a) 0.3Cu-0.3Ni steel, (b) 0.4Cu-0.4Ni steel, and (c) 0.7Cu-0.7Ni steel

3. Results and Discussion

3.1 Corrosion Test Results and Analysis of Corrosion Evolution Process

The curves of Fig. 1, calculated using Eq 1, show the change in the corrosion rate with time during the alternate immersion test simulating an industrial atmosphere. It can be seen that the corrosion rate of the three kinds of steel shows similar curves and declines quickly at the initial stage (before 144 h), followed by a small fluctuation in the stable stage. It is worth noting that the corrosion rates of the three kinds of steels differ in the initial stage of corrosion, but the differences decrease with increasing corrosion time, which indicates that the long-term corrosion behaviors of the steels follow a similar corrosion principle. However, after the corrosion tests, the corrosion rates of 0.4Cu-0.4Ni and 0.7Cu-0.7Ni steels remain low, while the 0.3Cu-0.3Ni steel showed a high corrosion rate. In the stable corrosion stage, the corrosion rate of 0.7Cu-0.7Ni steel is close to that of 0.4Cu-0.4Ni steel, indicating that the long-term corrosion resistances of the two kinds of steel are similar. The results of the three curves indicate that the corrosion rate is faster in the initial stage. Consequently, there were enough corrosion products produced on the sample surface that contributed to the improvement in corrosion protection in the stable stage.

The corrosion rates of the three types of steels in the immersion acceleration experiments containing S are above 2.0 mm a^{-1} at 48 h and about 1.12 mm a^{-1} at the range of 144-240 h. Results show that steel corrosion is more severe in the initial stage and becomes slower in the stable stage of the experiment. Reactions (1) and (3) correspond to the activities occurring in the initial and stable stage, respectively (Ref 10). Due to the rust layer, the initial reaction leads to a pH decline which speeds up corrosion, and the pH rise slows down corrosion due to oxidation at the later stage. These two different processes represent the change of corrosion products on the steel surface:

$$\text{Initial corrosion stage}: HSO_3^- + H_2O \rightarrow SO_3^{2-} + 3H^+ \quad \text{(Eq 2)}$$

$$\text{Stable corrosion stage}: SO_3^{2-} + O_2 + 2H^+ + 2e^- \rightarrow SO_4^{2-} + H_2O \quad \text{(Eq 3)}$$

Figure 2 shows the uniform macroscopic morphology of the steels before and after the removal of the rust layers after 240 h. The corrosion products on the surface of the three steel samples are dark brown and orange. According to the results from previous field exposure tests (Ref 4, 8), the color of the corrosion products of low carbon steel gradually deepens with longer exposure time. Inferring the results from Fig. 1, at the initial stage of corrosion, the rust layer may be too thin to resist the corrosion species, contributing to a high initial corrosion rate for all the steels. As corrosion time increases, the rust layer becomes denser, which protects the steel from the diffusion of O_2 molecules and reduces the corrosion rate (Ref 8). The rust layer also darkens or deepens in color. The outer rust layer formed on 0.3Cu-0.3Ni steel was not bonded well to the metal, making it easy to peel off, which exposed a light-yellow inner rust layer. Large valleys were found at the bottom part of the samples, which may be associated with the flow of electrolytes

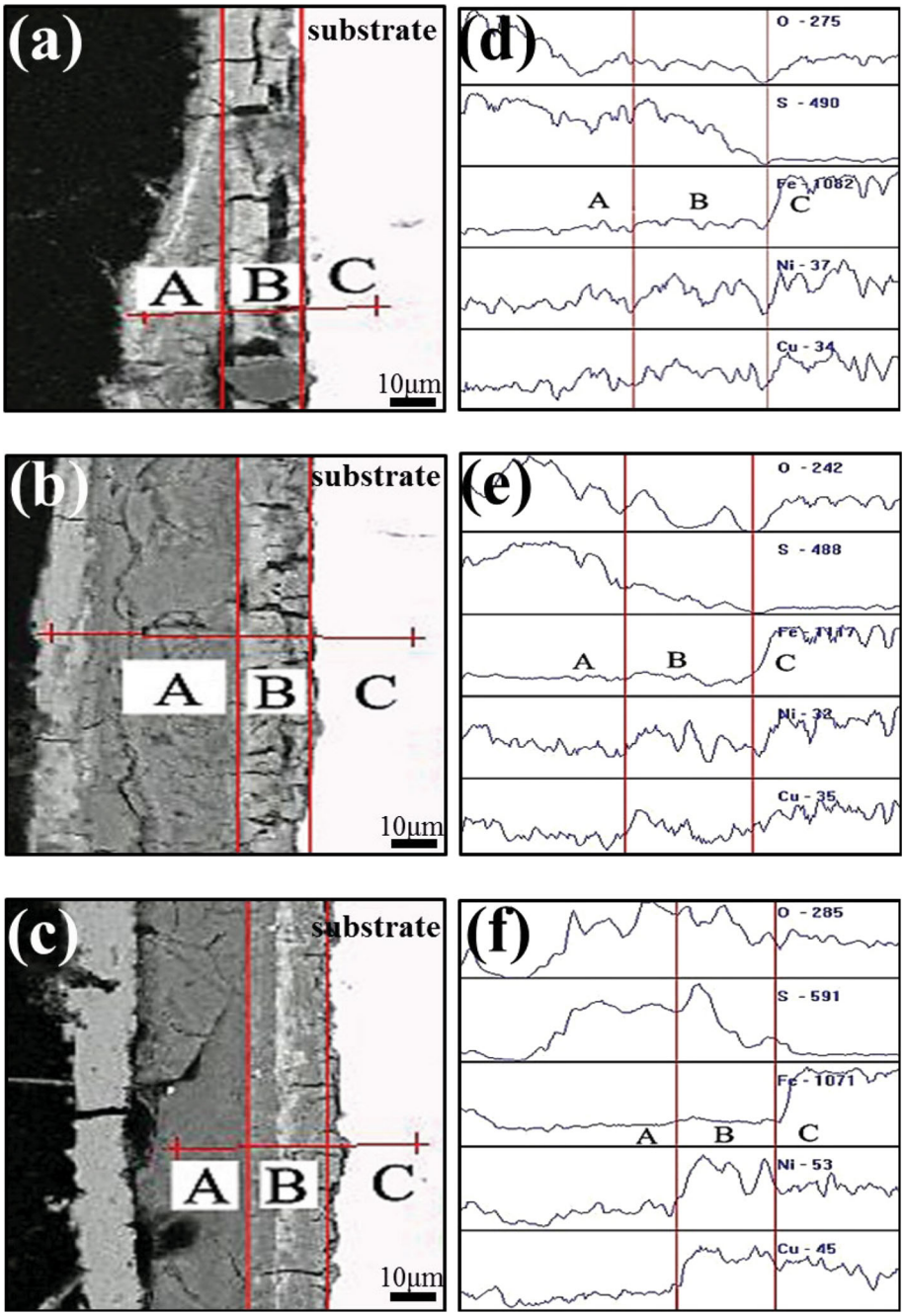

Fig. 4 Cross-sectional morphologies and EDS spectra of the corrosion products on the investigated steels after 240-h corrosion tests: (a, d) 0.3Cu-0.3Ni steel, (b, e) 0.4Cu-0.4Ni steel, and (c, f) 0.7Cu-0.7Ni steel

as samples were suspended and dried. After removing the rust layer, it can be found that all steels have completely developed into a hole comprehensive corrosion in the industrial atmosphere.

3.2 Characterization and Analysis of Corrosion Product

Figure 3 presents the micromorphology of the outer corrosion products after the entire duration of the alternate immersion tests. It can be seen that the rust layer of 0.3Cu-0.3Ni steel contains numerous large cracks and the rust layer is loose and easy to peel off, while the rust layers of 0.4Cu-0.4Ni and 0.7Cu-0.7Ni steels are relatively dense. The surface of the rust layer in the simulated industrial atmosphere environment, as shown in Fig. 3, mainly presented sandy and globular shape, which may be associated with the existence of lepidocrocite (γ-FeOOH) (Ref 6, 10). Meanwhile, the coverage area of γ-FeOOH on 0.3Cu-0.3Ni steel is less than the other steels. Thus, the rust layer on 0.3Cu-0.3Ni steel shows a more exposed surface where aggressive environmental agents (i.e., SO_3^{2-}, SO_4^{2-}, O_2) can attack the steel. Combined with the corrosion rate curves shown in Fig. 1, it can be inferred that a protective inner layer corrosion product was generated, in line with previous studies (Ref 8-10), and the addition of Cu and Ni alloy elements contributes to the formation and densification of the corrosion products, which is confirmed below.

Figure 4 shows the cross-sectional morphologies and EDS analyses of the corrosion products after the entire duration of alternate immersion tests. The cross-sectional morphologies of the rust layers in 0.4Cu-0.4Ni and 0.7Cu-0.7Ni steels are thicker compared with 0.3Cu-0.3Ni steel, which is consistent with their minor corrosion rates during the stable stage. EDS analysis results show that the rust layers of all steels present the element enrichment phenomenon, and the content of Cu, Ni alloy elements observed in the inner rust layer (partial B) is higher than the outer rust layer (partial A) and steel substrate (partial C). The element enrichments found in the corrosion products of 0.3Cu-0.3Ni and 0.4Cu-0.4Ni steels are not as evident as those of 0.7Cu-0.7Ni steel. Further, S introduced by $NaHSO_3$ electrolytes was observed with decreasing concentrations and decreasing distance to the matrix in the rust layer. It is inferred that the addition of Cu and Ni has remarkable effects on resisting the aggressiveness of corrosion pollutants present in industrial atmospheres, such as S. Previous works (Ref 6-8) have reported that the rusting process on steel progressed by the following corrosion processes in industrial atmospheres containing sulfur dioxide (SO_2):

$$4Fe + 4SO_2 + 5O_2 + 6H_2O \rightarrow 4FeOOH + 4H_2SO_4 \quad \text{(Eq 4)}$$

$$2H_2SO_4 + O_2 + 2Fe \rightarrow 2FeSO_4 + 2H_2O \quad \text{(Eq 5)}$$

The cyclic corrosion processes above present promotion of the transformation of FeOOH and the formation of a crack-free and protective rust layer accelerated by SO_2. In the present study, SO_2 can be produced from Eq 1 in the initial corrosion stage. The significant distinction of the element distribution of S between parts A and partial B, as shown in Fig. 4(a-1) indicates that ferrous sulfate ($FeSO_4$) is a part of the outer rust based on the EDS results of 0.3Cu-0.3Ni and 0.4Cu-0.4Ni steels shown in Fig. 4(d) and (e).

The XRD patterns of the inner rust layers are shown in Fig. 5(a). The proportion of α-FeOOH and CuO among the corrosion products were identified by semiquantitative analysis (about 10% relative errors) through X'pert Highscore Plus according to the Relative Intensity Ratio method (RIR) (Ref 19, 20). The results are presented in Fig. 5(b). The phase compositions of the inner rust layer corroded in the agents simulating industrial atmosphere are quite similar and mainly composed of α-FeOOH, γ-FeOOH, $FeSO_4{\cdot}nH_2O$, and CuO. α-FeOOH in the shape of needles or whiskers (Ref 14, 15, 21, 22] is a stable structure that is formed by the transformation of γ-FeOOH. Meanwhile, the presence of SO_2 in the acidic environment of corrosion pits promotes the formation of the stable phase of α-FeOOH (Ref 15). It can be seen from Fig. 5 that the mass fraction of α-FeOOH in the rust increased with the addition of Cu and Ni in steel. Previous studies have shown that the element contents of the rust layer affect the corrosion process of steel (Ref 11, 12, 16, 17). Therefore, inferring the result from Fig. 2, the stabilities of the rust layers on 0.4Cu-0.4Ni and 0.7Cu-0.7Ni steels are higher than those of 0.3Cu-0.3Ni weathering steel. It should be noted that the increased relative content of CuO is consistent with the content of Cu in steels. CuO has been formed and enriched in the inner rust layer, which can retard the growth and densify the rust to suppress the diffusion of O_2 to the steel surface. Compared with the distribution of S in the EDS results, shown in Fig. 4, it can be concluded that the CuO and Ni compounds may reduce the penetration of aggressive electrolytes to the steel surface.

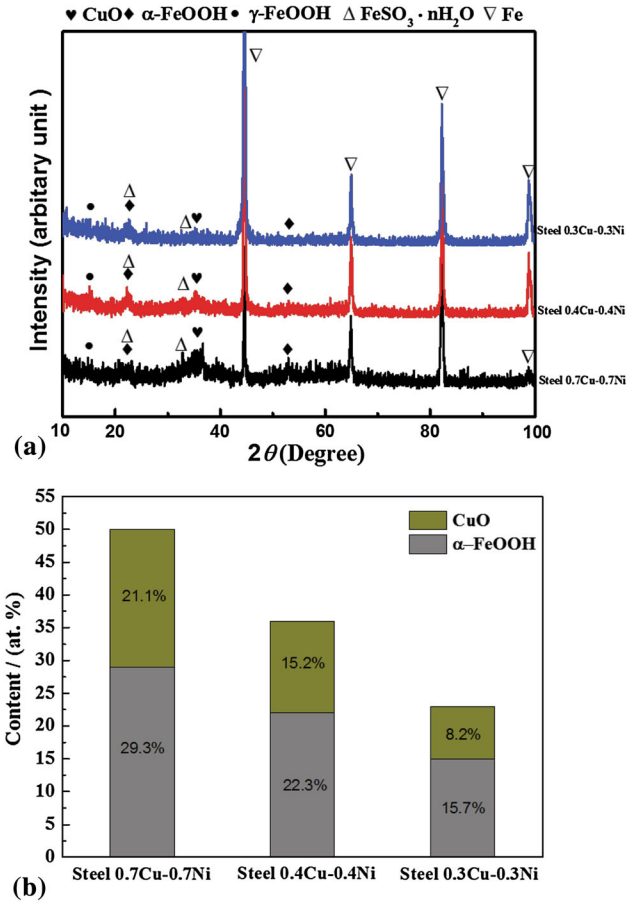

Fig. 5 (a) XRD patterns of the corrosion products and the (b) semiquantitative analysis for CuO and α-FeOOH of the corrosion products formed on the steels after 240-h corrosion tests

3.3 Effects of Cu and Ni on the Electrochemical Experiments

Figure 6 shows the Nyquist plots of the three bare steel plates in 0.085 mol/L $NaHSO_3$ solution under OCP (Open Circuit Potential) conditions and the electrical equivalent circuit applied for fitting the EIS parameters listed in Table 3. The

Table 3 Equivalent circuit parameters for impedance spectra of the three bare steels in 0.085 mol/L $NaHSO_3$ solution under OCP conditions

Materials	R_s, Ω cm^2	Q_{dl}, Ω^{-1} cm^{-2} S^n	n_{dl}	R_{ct}, Ω cm^2	R_{film}, Ω cm^2	n_{dl}	Q_{film}, Ω^{-1} cm^{-2} S^n
Steel 0.3Cu-0.3Ni	5.2	2.03E−05	0.66	151.8	16.1	0.74	3.52E−04
Steel 0.4Cu-0.4Ni	7.5	3.31E−05	0.65	288.1	36.1	0.68	5.20E−04
Steel 0.7Cu-0.7Ni	7.4	4.42E−05	0.64	304.2	45.6	0.71	7.54E−04

small χ^2 value ($\sim 10^{-3.5}$, an order of magnitude) suggests a good fitting of the results. It can be inferred that the impedance spectrum reveals two typical capacitance loops: one larger, low-frequency capacitive loop resulted from a small amount of the corrosion products initially formed on the surface of the specimen, and the other smaller, high-frequency capacitive loop resulted from the charge transfer resistance at the specimen–solution interface. In the case of the electrical equivalent circuit, shown in Fig. 6, R_{film} and R_s are corrosion product film resistance and solution resistance, respectively. Q_{dl}, which is used to replace the pure capacitance element to reflect the capacitance behavior (Ref 21), and R_{ct} are the double-layer capacitance and charge transfer resistance, respectively. The values of n_{dl} are approximately 0.65, suggesting that Q_{dl} exhibits intermediate properties between a pure capacitor and a Warburg impedance element. Q_{film} reflects the electrochemical response of the corrosion film product, and the values of n_{film} were approximately 0.7 (Ref 21-23).

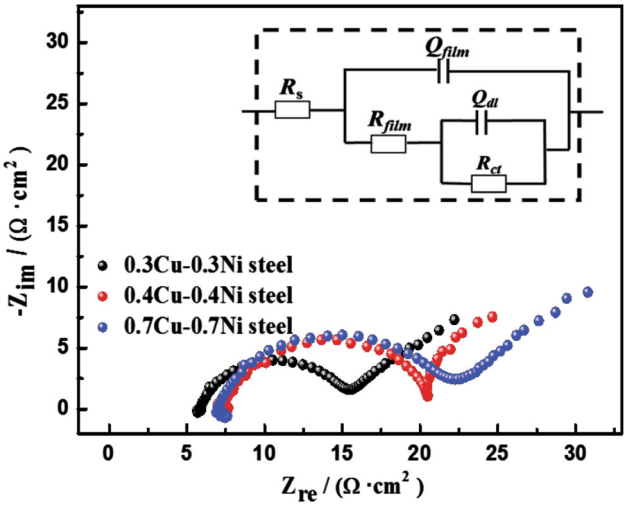

Fig. 6 Nyquist plots of the investigated steels tested in a 0.085 mol/L $NaHSO_3$ solution

As shown in the fitted results listed in Table 3, R_{ct} can be used to reflect the changes in the interfacial reaction resistance used to compare the corrosion rate, and the R_{ct} values gradually increase with the increase in the content of Cu and Ni in steel. The charge transfer passages were blocked caused by the increase of R_{ct}. Consequently, the corrosion rate decreased correspondingly to the initial corrosion stage of Fig. 1. The R_{film} values present the same tendency with R_{ct}, which indicates that the addition of alloying elements in steel increases the surface coverage of the rust layers formed by reactions (4, 5).

Figure 7 represents the Nyquist plots of the three steel specimens in 0.085 mol/L $NaHSO_3$ solution under OCP (Open

Table 4 Fitted values of the elements in the equivalent circuit of 0.3Cu-0.3Ni steel tested at different corrosion times in a 0.085 mol/L $NaHSO_3$ solution

Corrosion time, day	R_s, Ω cm^2	R_{pore}, Ω cm^2	Q_{film}, Ω^{-1} cm^{-2} S^n	n_1	Q_{dl}, Ω^{-1} cm^{-2} S^n	n_2	R_{ct}, Ω cm^2
2	6.20	56.00	5.83E−03	0.72	1.43E−03	0.87	51.80
4	8.70	62.00	5.42E−03	0.73	1.12E−02	0.67	62.30
6	6.10	73.00	7.28E−03	0.71	1.87E−02	0.65	243.20
8	5.50	101.00	1.92E−02	0.65	1.93E−02	0.64	367.20
10	4.90	103.00	2.26E−02	0.64	1.35E−02	0.56	395.20

Table 5 Fitted values of the elements in the equivalent circuit of 0.4Cu-0.4Ni steel tested at different corrosion times in a 0.085 mol/L $NaHSO_3$ solution

Corrosion time, day	R_s, Ω cm^2	R_{pore}, Ω cm^2	Q_{film}, Ω^{-1} cm^{-2} S^n	n_1	Q_{dl}, Ω^{-1} cm^{-2} S^n	n_2	R_{ct}, Ω cm^2
2	10.12	61.00	4.83E−03	0.74	3.16E−03	0.78	58.00
4	9.23	63.21	6.32E−03	0.72	6.93E−03	0.71	64.60
6	7.92	79.23	7.53E−03	0.71	2.00E−02	0.68	281.20
8	12.31	110.10	1.72E−02	0.66	1.98E−02	0.69	390.40
10	5.97	116.00	2.06E−02	0.65	1.37E−02	0.59	402.30

Table 6 Fitted values of the elements in the equivalent circuit of 0.7Cu-0.7Ni steel tested at different corrosion times in a 0.085 mol/L $NaHSO_3$ solution

Corrosion time, day	R_s, Ω cm^2	R_{pore}, Ω cm^2	Q_{film}, Ω^{-1} cm^{-2} S^n	n_1	Q_{dl}, Ω^{-1} cm^{-2} S^n	n_2	R_{ct}, Ω cm^2
2	17.30	71.00	5.70E−03	0.73	3.30E−03	0.78	67.30
4	12.20	78.00	6.63E−03	0.72	7.25E−03	0.71	72.10
6	10.81	91.30	1.03E−02	0.69	2.06E−02	0.68	293.20
8	10.92	132.54	2.60E−02	0.64	2.03E−02	0.69	412.00
10	6.71	181.32	5.32E−02	0.61	1.55E−01	0.59	483.56

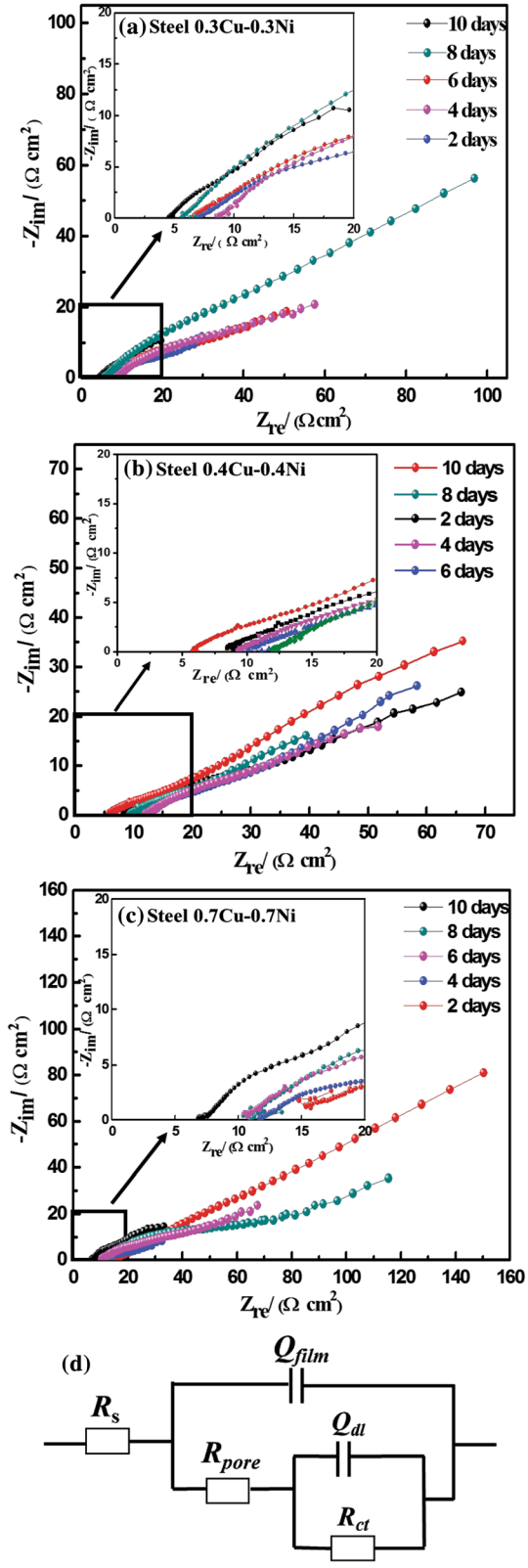

Fig. 7 (a) Nyquist plots of 0.3Cu-0.3Ni, (b) 0.4Cu-0.4Ni, and (c) 0.7Cu-0.7Ni steels tested at different corrosion times in a 0.085 mol/L $NaHSO_3$ solution and (d) the equivalent circuit used for fitting the EIS results

Circuit Potential) conditions after immersion tests with different corrosion times and the corresponding electrical equivalent circuit. The enlarged portion (20 Ω cm^{-2} × 20 Ω cm^{-2}) of each plot is inserted into the corresponding graph. In the electrical equivalent circuit, R_s is the electrolyte solution resistance. Q_{dl} and R_{ct} are chosen to fit the electric double-layer capacitance and resistance, respectively. The terms Q_{film} and R_{pore} represent the corrosion film capacitance and the resistance of the pores in the corrosion products, respectively. The electrical element parameters obtained from fitting the EIS data are listed in Tables 4, 5, and 6.

The Nyquist plots display similar features where a capacitive semicircle covers most of the high-frequency region and a straight line goes through the low-frequency domain (Ref 24-30). The plots show that as the corrosion time of immersion tests increases, the electrochemical capacitance semicircle radius of the steel also increases. Accordingly, the capacitance arc radius is related to the corrosion resistance of the rust layer on the surface of the steels (Ref 23, 31). Q_{film} listed in Tables 4, 5, and 6 gradually increases with the extension of the immersion time, which verifies that the cover ratio of the corrosion products on the substrate surfaces and the protective characters of the corrosion products increased. The R_{pore} parameter was used instead of the Warburg impedance (W) to describe the mass transport process in the pore located in the corrosion products (Ref 21-23). The value of R_{pore} increases with the increase in immersion time, which indicates a denser rust layer. Compared with the EIS fitting parameters of three steels listed in Tables 4, 5, and 6, the value of the charge transfer resistance (R_{ct}) increases with the addition of Cu and Ni in steel, suggesting higher reaction resistance values can be obtained on the steel surface, consistent with the results of Fig. 6. Meanwhile, the increase in the R_{pore} value in 0.4Cu-0.4Ni and 0.7Cu-0.7Ni steels suggests the compactness of the corrosion films increases with the addition of Cu and Ni.

Thus, combined with the results of XRD patterns and cross-section EDS, it can be inferred that the pores in the corrosion products were blocked by the formation of CuO or Ni compounds, and the initial corrosion products with $FeSO_4$ precipitated on the steel surface protected the substrate when exposed to industrial atmosphere environment. The formation of $FeSO_4$ increases the R_{ct} values by reducing the number of active sites on the steel surface. As some studies have reported (Ref 19, 32), the protection provided by a corrosion film is closely associated with its porosity since the corrosion medium can react with steel through the pores in the corrosion products. Additionally, the protection provided by the corrosion film is also related to its porosity aside from its thickness. Hence, if the corrosion products could not completely obstruct the corrosive medium, numerous active sites would penetrate to the steel surface to undermine the corrosion film and substrate. Thus, as the Cu and Ni content increase, it may be sufficient to form CuO or Ni compounds to effectively cover the pores making the corrosion products substantially denser (Fig. 8). These findings further indicate that the corrosion process of the mild steel is controlled by a charge transfer process and a diffusion control process in the $NaHSO_3$ solution.

Figure 9 shows the linear polarization curves of three bare steels and the steels with the rust layer after 240-h alternate immersion tests. Linear polarization can acquire a steady-state

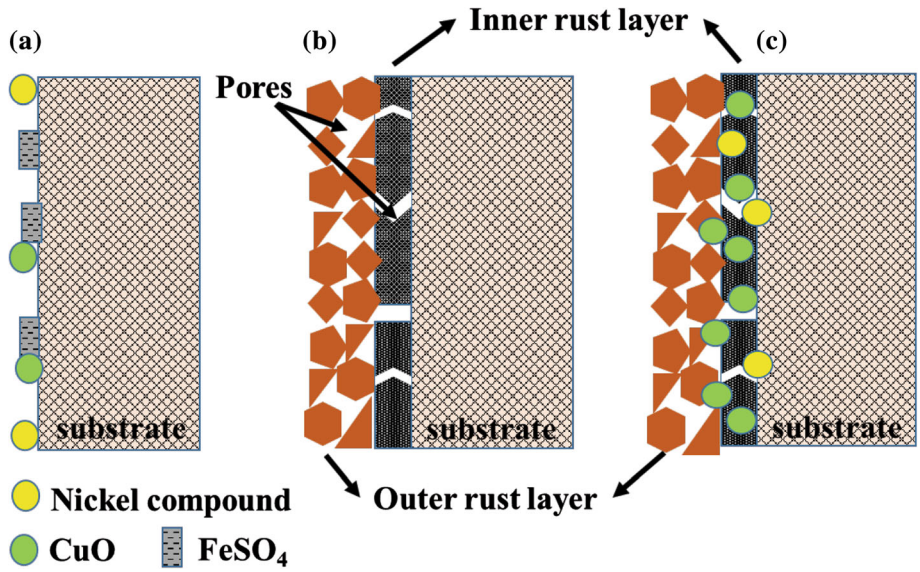

Fig. 8 (a) Corrosion mechanism for Cu-Ni mild steel alloys at the beginning of the corrosion process in a 0.085 mol/L $NaHSO_3$ solution, and the (b) schematic of the evolution mechanisms of the corrosion products in steels with low and high Cu-Ni content, respectively

Table 7 Parameters obtained from the linear polarization curves

	Steels without rust		Steels with rust	
Steels	E_{corr} vs. SCE, mV	R_P, Ω cm^2	E_{corr} vs. SCE, mV	R_P, Ω cm^2
Steel 0.3Cu-0.3Ni	− 660.2	45.49	− 614.1	100.9
Steel 0.4Cu-0.4Ni	− 650.1	48.64	− 598.7	106.9
Steel 0.7Cu-0.7Ni	− 625.9	49.34	− 583.4	106.2

polarization curve in the micropolarization region (± 10 mV) near the corrosion potential (Ref 13). According to the Stern equation (Ref 32):

$$i_{corr} = \frac{\beta_a \beta_c}{2.303(\beta_a + \beta_{c)}} \times \frac{1}{R_p} \quad \text{(Eq 6)}$$

where β_a and β_c are anodic cathodic reaction Tafel constants, respectively, and R_p is the polarization resistance, which can be obtained from linear polarization curves. The parameter values were calculated using Eq 6, and the results are listed in Table 7. It can be seen that the curves in Fig. 9 show similar results, and both Tafel constants fluctuate slightly. The corrosion potential increases with the addition of Cu and Ni in steel, which verifies that these elements can improve the corrosion resistance of mild steels. Compared with bare steels, linear polarization curves of the steels with rust layers show higher corrosion potentials and polarization resistances, suggesting a protective products film was formed on the steel substrate surface. The increases in R_p and E_{corr} (versus SCE) for 0.4Cu-0.4Ni and 0.7Cu-0.7Ni steels with rust indicate that Cu and Ni improve the corrosion resistance of the rust layer. Therefore, mild steels show lower corrosion rates with increasing Cu and Ni as indicated in Fig. 1.

4. Conclusions

The corrosion behaviors of Cu-Ni mild steels in alternate immersion accelerated tests simulating a corrosive industrial atmosphere at different times have been investigated resulting in the following conclusions:

1. The low-alloy steels showed two stages in the whole alternate immersion corrosion process, and the corrosion rates decelerate faster in the initial stage than that in the stable stage.
2. As the corrosion process proceeds, the protection provided by the rust layer on the steel surface was increased. In addition, the Cu and Ni concentrations increased in the inner rust layer. CuO and $FeSO_4{\cdot}nH_2O$ were detected in the rust layers of the investigated steels.
3. The rust layers became compact and crack-free with the addition of Cu and Ni. CuO or Ni filled the pores of the rust layer which improved the corrosion resistance. Thus, it is feasible to increase the content of Cu and Ni in WS to increase the resistance of steels used in corrosive industrial environments.

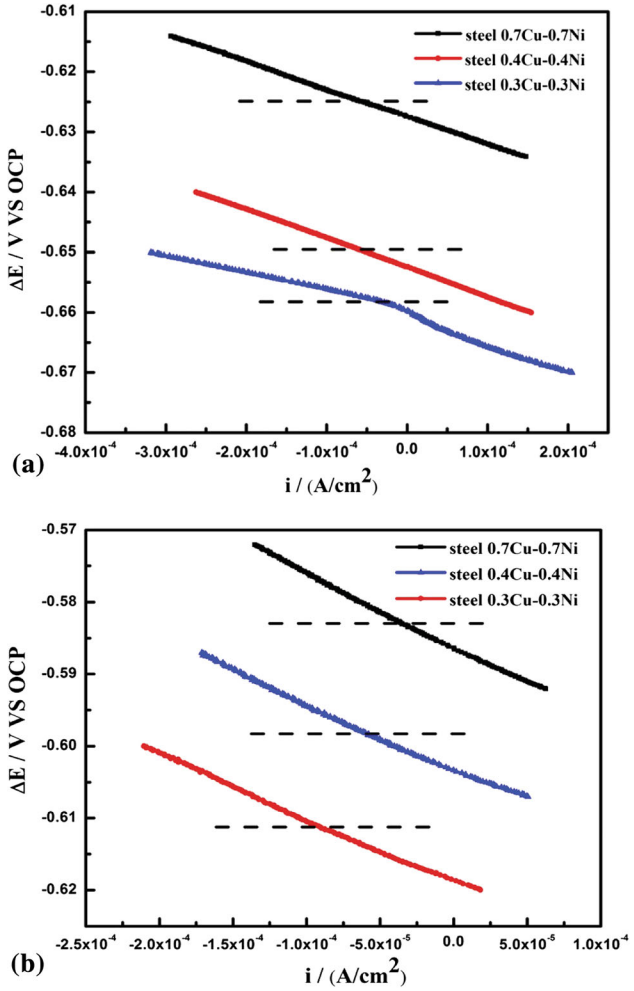

Fig. 9 Linear polarization curves of (a) the three bare steels and (b) steels with rust layers after 240-h alternate immersion tests

Acknowledgments

The authors acknowledge the support from National Key R&D Program of China (2016YFE0203600) and National Natural Science Foundation of China (51571027).

References

1. R. Rihan, R. Shawabkeh, and N. Al-Bakr, The Effect of Two Amine-Based Corrosion Inhibitors in Improving the Corrosion Resistance of Carbon Steel in Sea Water, *J. Mater. Eng. Perform.*, 2014, **23**(3), p 693–699
2. J. Gu, Y. Xiao, N. Dai, X. Zhang, Q. Ni, and J. Zhang, The Suppression of Transformation of γ-FeOOH to α-FeOOH Accelerating the Steel Corrosion in Simulated Industrial Atmosphere Environment with a DC Electric Field Interference, *Corros. Eng. Sci. Technol.*, 2019, **54**(3), p 249–256
3. S. Sabir and A.A. Ibrahim, Influence of Atmosphere Pollution on Corrosion of Materials in Saudi Arabia, *Corros. Eng. Sci. Technol.*, 2017, **52**(4), p 276–282
4. Z. Malaibari, R. Kahraman, H. Saricimen, and A. Quddus, Investigation of Atmosphere Corrosion of Mild Steel After Treatment by Several Inhibitor Solutions, *Corros. Eng. Sci. Technol.*, 2013, **42**(2), p 112–118
5. Z. Feng, X. Cheng, C. Dong, L. Xu, and X. Li, Passivity of 316L Stainless Steel in Borate Buffer Solution Studied by Mott-Schottky Analysis, Atomic Absorption Spectrometry and X-ray Photoelectron Spectroscopy, *Corros. Sci.*, 2010, **52**(11), p 3646–3653
6. D. Krouse, N. Laycock, and C. Padovani, Modelling Pitting Corrosion of Stainless Steel in Atmosphere Exposures to Chloride Containing Environments, *Corros. Eng. Sci. Technol.*, 2014, **49**(6), p 521–528
7. S. Topolska, Investigation of Corrosion of Welded Joints of Austenitic and Duplex Stainless Steels, *IOP Conf. Ser. Mater. Sci. Eng.*, 2016, **145**(7), p 072014
8. C. Pan, M. Guo, W. Han, Z. Wang, and C. Wang, Study of Corrosion Evolution of Carbon Steel Exposed to an Industrial Atmosphere, *Corros. Eng. Sci. Technol.*, 2019, **54**(3), p 241–248
9. Z. Wang, J. Liu, L. Wu, R. Han, and Y. Sun, Study of the Corrosion Behavior of Weathering Steels in Atmosphere Environments, *Corros. Sci.*, 2013, **67**, p 1–10
10. Z.X. Yang, B. Kan, J.X. Li, Y.J. Su, and L.J. Qiao, Hydrostatic Pressure Effects on Corrosion Behavior of X70 Pipeline Steel in a Simulated Deep-Sea Environment, *J. Electroanal. Chem.*, 2018, **822**, p 123–133
11. M. Rajabi, R. Miresmaeili, and M. Aliofkhazraei, Hardness and Wear Behavior of Surface Mechanical Attrition Treated Titanium, *Mater. Res. Express*, 2019, **6**(6), p 065003
12. C. Ma, S. Song, Z. Gao, J. Wang, W. Hu, Y. Behnamian, and D.-H. Xia, Electrochemical Noise Monitoring of the Atmosphere Corrosion of Steels: Identifying Corrosion form Using Wavelet Analysis, *Corros. Eng. Sci. Technol.*, 2017, **52**(6), p 432–440
13. M.N. Nguyen, X. Wang, and R.H. Leicester, An Assessment of Climate Change Effects on Atmosphere Corrosion Rates of Steel Structures, *Corros. Eng. Sci. Technol.*, 2013, **48**(5), p 359–369
14. M. Natesan, S. Selvaraj, T. Manickam, and G. Venkatachari, Corrosion Behavior of Metals and Alloys in Marine-Industrial Environment, *Sci. Technol. Adv. Mater.*, 2008, **9**(4), p 045002
15. M.C.L. De Oliveira, V.S.M. Pereira, O.V. Correa et al., Corrosion Performance of Anodized AZ91D Magnesium Alloy: Effect of the Anodizing Potential on the Film Structure and Corrosion Behavior, *J. Mater. Eng. Perform.*, 2014, **23**(2), p 593–603
16. L.N. Xu, J.Y. Zhu, M.X. Lu, Z. Lei, and C. Wei, Electrochemical Impedance Spectroscopy Study on the Corrosion of the Weld Zone of 3Cr Steel Welded Joints in CO_2 Environments, *Int. J. Miner. Metall. Mater.*, 2015, **22**(5), p 500–508
17. K.G. Mishra and C.R. Das, Corrosion of Welded Steel Specimens in Industrial Steel Plant Atmospheres, *Br. Corros. J.*, 1987, **22**(3), p 195–198
18. S. Guo, L. Xu, Z. Lei, C. Wei, and M. Lu, Corrosion of Alloy Steels Containing 2% Chromium in CO_2 Environments, *Corros. Sci.*, 2012, **63**, p 246–258
19. Q.H. Zhao, W. Liu, Y.C. Zhu et al., Effect of Small Content of Chromium on Wet-Dry Acid Corrosion Behavior of Low Alloy Steel, *Acta Metall. Sin. (Engl. Lett.)*, 2017, **30**(2), p 164–175
20. M. Morcillo, B. Chico, J. Alcántara et al., SEM/Micro-Raman Characterization of the Morphologies of Marine Atmosphere Corrosion Products Formed on Mild Steel, *J. Electrochem. Soc.*, 2016, **163**(8), p 426–439
21. C. Pan, M. Guo, and Z. Wang, Effect of $MgCl_2$ on the Corrosion Behavior of Copper Under Periodic Wet/Dry Cycle Condition, *J. Mater. Eng. Perform.*, 2019, **28**(5), p 2562–2572
22. D. Kong, C. Dong, X. Ni et al., The Passivity of Selective Laser Melted 316L Stainless Steel, *Appl. Surf. Sci.*, 2020, **504**, p 144495
23. T. Zhang, J. Wu, L. Jin et al., Enhancing the Mechanical and Anticorrosion Properties of 316L Stainless Steel Via a Cathodic Plasma Electrolytic Nitriding Treatment with Added PEG, *J. Mater. Sci. Technol.*, 2019, **35**(11), p 2630–2637
24. D.C. Kong, C.F. Dong, X.Q. Ni et al., Insight into the Mechanism of Alloying Elements (Sn, Be) Effect on Copper Corrosion During Long-Term Degradation in Harsh Marine Environment, *Appl. Surf. Sci.*, 2018, **455**, p 543–553
25. X.Q. Cheng, Z. Jin, M. Liu et al., Optimizing the Nickel Content in Weathering Steels to Enhance Their Corrosion Resistance in Acidic Atmospheres, *Corros. Sci.*, 2017, **115**, p 135–142
26. D. Kong, C. Dong, X. Ni, and L. Zhang, High-Throughput Fabrication of Nickel-Based Alloys with Different Nb Contents via a Dual-Feed Additive Manufacturing System: Effect of Nb Content on Microstructural and Mechanical Properties, *J. Alloy. Compd.*, 2019, **785**, p 826–837
27. D. Kong, X. Ni, and C. Dong, Heat Treatment Effect on the Microstructure and Corrosion Behavior of 316L Stainless Steel

Fabricated by Selective Laser Melting for Proton Exchange Membrane Fuel Cells, *Electrochim. Acta*, 2018, **276**, p 293–303
28. D. Kong, X. Ni, and C. Dong, Bio-functional and Anti-corrosive 3D Printing 316L Stainless Steel Fabricated by Selective Laser Melting, *Mater. Des.*, 2018, **152**, p 88–101
29. D.C. Kong, A.N. Xu, and C.F. Dong, Electrochemical Investigation and Ab Initio Computation of Passive Film Properties on Copper in Anaerobic Sulphide Solutions, *Corros. Sci.*, 2017, **116**, p 34–43
30. D. Kong, C. Dong, and X. Ni, Corrosion of Metallic Materials Fabricated by Selective Laser Melting, *Npj Mater. Degrad.*, 2019, **3**, p 1–13
31. Z.F. Yin, X.Z. Wang, L. Liu et al., Characterization of Corrosion Product Layers from CO_2 Corrosion of 13Cr Stainless Steel in Simulated Oilfield Solution, *J. Mater. Eng. Perform.*, 2011, **20**(7), p 1330–1335
32. S. John, A. Salam, A.M. Baby, and A. Joseph, Corrosion Inhibition of Mild Steel Using Chitosan/TiO_2 Nanocomposite Coatings, *Prog. Org. Coat.*, 2019, **129**, p 254–259